# Cross-Correlation Analysis of Long-Term Ambient Seismic-Noise Recordings in the Caribbean Netherlands to Monitor the Volcanoes on Saba and St. Eustatius

Reinoud Sleeman*[1] and Elske de Zeeuw-van Dalfsen[1]

## ABSTRACT

**The continuous recordings of broadband seismometers on Saba and St. Eustatius in the Lesser Antilles provide a unique and long data set to measure temporal seismic velocity variations (*dv/v*) at two active but quiescent volcanoes (Mt. Scenery and The Quill). We compare results from single-station cross-component (SC) correlations with cross-station cross-component (CC) correlations and achieve the best similarities within the frequency band 1.3–2.1 Hz, with average correlations of 0.82 for Saba and 0.36 for St. Eustatius, justifying the use of SC as proxy for CC at these frequencies. Temporal *dv/v* variations derived from 13 yr of data show different characteristics at both islands. At St. Eustatius *dv/v* highly correlates (0.72) with air temperature and can be modeled by a simple sine wave with a period of 1 yr. Remaining residuals reveal cohurricane *dv/v* drops, thus at times of the passage of a hurricane. At Saba, subsurface velocity variations show temporal coseismic changes, up to −0.49% compared with −0.19% at St. Eustatius, and thus show a higher sensitivity to ground shaking. Our data set, although limited, shows a linear relation (correlation 0.78) between the coseismic *dv/v* drop and peak ground velocity at Saba around 1.3 Hz. We model the associated seismic velocity recovery with an exponential decay function and we estimate the recovery time at 2 yr. After subtracting the coseismic drop and recovery model, *dv/v* at Saba obtained from CC data correlates with the sine model (correlation 0.71). SC may be an appealing alternative for CC for monitoring purposes; however, the use of a small network is preferred to reduce the variance in *dv/v* (at St. Eustatius from 0.12% to 0.05%) and to detect *dv/v* variations unrelated to volcanic activity (e.g., hurricane). We continue work on the implementation of CC in the daily monitoring for Mt. Scenery and The Quill.**

## KEY POINTS

- We determine seismic velocity variations to monitor the Caribbean volcanoes Mt. Scenery and The Quill.
- Subsurface velocity at The Quill is mainly sensitive to air temperature and at Mt. Scenery to ground shaking.
- A small seismic network is effective for detecting velocity variations even if unrelated to volcanic activity.

## INTRODUCTION

The Caribbean Netherlands consists of three islands in the Caribbean Sea: Bonaire, St. Eustatius, and Saba, which are also referred to as the BES islands. Saba and St. Eustatius are located east of Puerto Rico and are part of the Lesser Antilles. Bonaire is located on the southern part of the Caribbean plate and is not part of this study.

The Lesser Antilles island arc can be divided into two categories of islands based on geology and tectonic setting (Maury *et al.*, 1991): the outer Leeward islands (outer arc) and the inner Leeward islands (inner arc) (Fig. 1). St. Maarten, an autonomous state within the Kingdom of the Netherlands, is located in the outer extinct volcanic arc, which ceased to erupt about 18 million years ago (Allen *et al.*, 2019). Saba and St. Eustatius are located in the northernmost part of the active inner arc and host active volcanoes: Mt. Scenery

1. KNMI, De Bilt, The Netherlands

*Corresponding author: sleeman@knmi.nl

**Cite this article as** Sleeman, R., and E. de Zeeuw-van Dalfsen (2020). Cross-Correlation Analysis of Long-Term Ambient Seismic-Noise Recordings in the Caribbean Netherlands to Monitor the Volcanoes on Saba and St. Eustatius, *Bull. Seismol. Soc. Am.* **XX**, 1–18, doi: 10.1785/0120200011

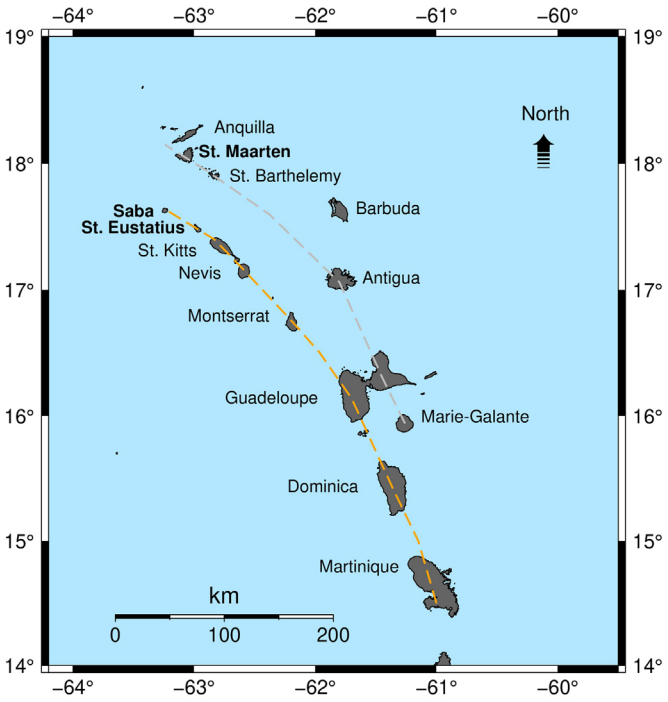


**Figure 1.** Geographical map of the Lesser Antilles islands. The islands of the active inner arc (southern dashed line) are built of igneous rocks and the islands of the outer arc (northern dashed line) consist of igneous rocks covered by limestone. The color version of this figure is available only in the electronic edition.

on Saba and The Quill on St. Eustatius. Since 2006, the Royal Netherlands Meteorological Institute (KNMI) has deployed seismic network NA (de Zeeuw-van Dalfsen and Sleeman, 2018; see Data and Resources) to monitor seismicity on and around these three islands.

Volcanism in the whole outer arc started about 40 million years ago (Garmon *et al.*, 2017) and the arc consists of the following islands from north to south: Anguilla, St. Maarten, St. Barthelemy, Barbuda, Antigua, La Desirade, Grande Terre (Guadeloupe), and Marie-Galante. These islands consist of igneous rocks capped with limestone (Christman, 1953; Allen *et al.*, 2019).

The islands of the inner arc are Saba, St. Eustatius, St. Kitts and Nevis, Montserrat, Basse Terre (of Guadeloupe), Dominica, Martinique, St. Lucia, St. Vincent, the Grenadines, and Grenada. They are younger, about 20 million years old, and all host active volcanoes (Garmon *et al.*, 2017). This inner arc marks the current site of subduction of the North and South American plates under the Caribbean plate (Garmon *et al.*, 2017). Saba and St. Eustatius, at the northern end of the arc, have numerous pyroclastic deposits that reflect the explosive volcanic eruption history. The complex geology of Saba and St. Eustatius is described in detail by Westerman and Kiel (1961) and Roobol and Smith (2004).

Even though The Quill and Mt. Scenery have not erupted recently, they classify in the high to very high threat category (de Zeeuw-van Dalfsen and Sleeman, 2018). KNMI has monitored the volcanoes (de Zeeuw-van Dalfsen and Sleeman, 2018) using a network of broadband seismometers since 2006, Global Navigation Satellite Systems stations since 2018, and temperature probes in a hot spring on Saba also since 2018. Here, we consider the use of the seismic-waveform cross-correlation technique as a possible volcano monitoring tool.

Seismic ambient-noise data are increasingly used to study active volcanoes by analyzing temporal variations in cross-correlations of ambient noise recorded by pairs of seismometers (e.g., Sens-Schönfelder and Wegler, 2006; Brenguier *et al.*, 2008, 2011; Duputel *et al.*, 2009; Mordret *et al.*, 2010; Caudron *et al.*, 2015; Rivet *et al.*, 2015; Donaldson *et al.*, 2017; Machacca *et al.*, 2019), in particular from large and dense networks of broadband stations. The cross-correlation of ambient noise recorded by two seismometers yields an approximation of the Green's function (Shapiro and Campillo, 2004; Draganov *et al.*, 2006; Wapenaar and Fokkema, 2006) of which variations in time may indicate a change in seismic properties of the medium, such as wave propagation velocity, attenuation, and scattering (Aoki, 2015).

Multiple studies document coseismic velocity drops after earthquakes, followed by slow recovery (e.g., Rubinstein and Beroza, 2005; Brenguier *et al.*, 2008; Wegler *et al.*, 2009; Nakata and Snieder, 2011; Hobiger *et al.*, 2016; Hong *et al.*, 2017). A linear relationship between the local peak ground acceleration (PGA) due to an earthquake and the corresponding seismic velocity change was observed by Richter *et al.* (2014). Ikeda and Tsuji (2018) observed that the coseismic velocity drop tended to increase with increasing peak ground velocity (PGV). Furthermore, seismic velocity variations were observed before the onset of volcanic eruptions and attributed to the intrusion of magmatic fluids and the opening of fractures (e.g., Bennington *et al.*, 2018; Olivier *et al.*, 2019) and after tremors (Ballmer *et al.*, 2013). Temporal variations related to seasonal effects have also been recognized (e.g., Sens-Schönfelder and Wegler, 2006; Meier *et al.*, 2010; Gassenmeier *et al.*, 2015; Hillers *et al.*, 2015). Sources of these seasonal variations are found in thermoelastic and hydrologic effects, as well as in the annual snow cycle (Hotovec-Ellis *et al.*, 2014).

The approximation of the retrieved Green's functions may be influenced by (1) directivity (change in the location) of noise sources (e.g., ocean-generated noise; Froment *et al.*, 2010; Hanasoge, 2013), (2) the contribution from transient signals (e.g., from earthquakes and storms) or localized sources, and (3) timing errors or other instrumental errors (Stehly *et al.*, 2007; Sens-Schönfelder, 2008). The effect of these types of contamination may be reduced, or eliminated, by data selection (e.g., removing outliers and data with poor data quality), disregarding signal amplitudes (e.g., Bensen *et al.*, 2007), and stacking of cross-correlations over a long time period (e.g., months to years) to account for nonstationarity of the noise

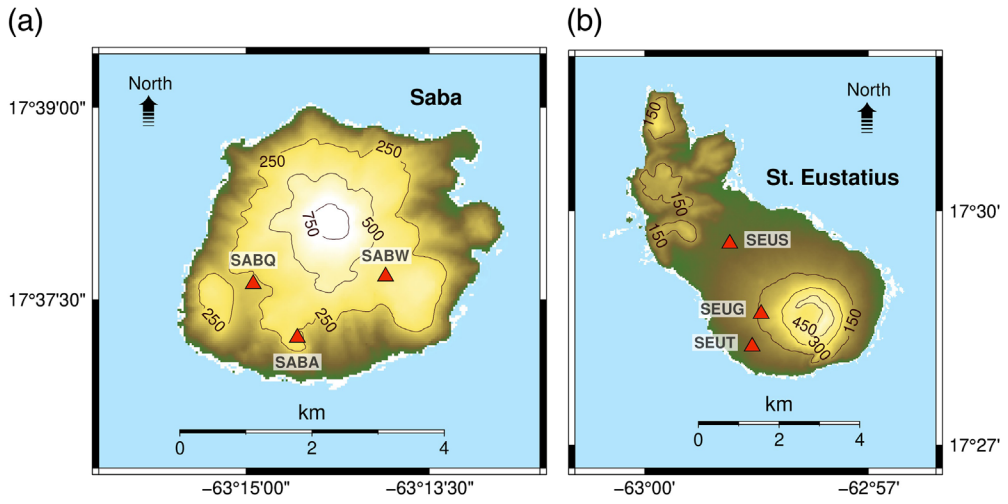


**Figure 2.** Seismometers of network NA at (a) Saba and (b) St. Eustatius. The background is the Shuttle Radar Topography Mission digital elevation model with elevation contours in meters. The color version of this figure is available only in the electronic edition.

(Hadziioannou *et al.*, 2009). Finally, the data processing applied to obtain seismic-noise cross-correlation functions (CCFs) is critical and may influence the results (Groos *et al.*, 2012). The cross-correlation coefficient with respect to the reference cross-correlation (RefCC) is indicative for the quality of the data and the processing (e.g., Hadziioannou *et al.*, 2009; Fokker and Ruigrok, 2019). The interpretation of changes in the cross-correlations over time remains a challenge due to complexities arising when separating time shifts due to physical change in the medium from those related to instrumental effects and/or changes in ambient-noise source distribution (Hable *et al.*, 2018). In this context, we discuss in this article the identification of data quality issues (e.g., timing and tilted sensor) and of nonstationarity of noise as sources of contamination.

The cross-correlation technique typically uses data from pairs of stations; however, a number of recent studies also show the applicability of cross-correlation between the different components of a single station (e.g., de Plaen *et al.*, 2016; Hobiger *et al.*, 2016), hence providing an alternative in monitoring volcanic activity using a single three-component sensor only.

In this article, we apply the cross-correlation technique on seismic data from the NA network with the goal to determine the base level of seismic velocity variations at Saba, St. Eustatius, and St. Maarten, using 13 yr of data, and to understand their characteristics. First, we carefully analyze the seismic data for quality issues and discard all data that do not fit our criteria. Then, we apply the cross-correlation technique to each station–channel pair combination at both Saba and St. Eustatius in different frequency bands and analyze the similarities to select the frequency band that justifies the use of single-station cross-component (SC) correlations as proxy for the cross-station correlations. We then show the results of the SC analysis for stations SABA on Saba, SEUS on St. Eustatius, and SMRT on St. Maarten using 13 yr of data, which essentially provide the base level of the seismic velocity variations. To understand the characteristics of this base level, we correlate the data with various meteorological parameters and investigate the dependency with temporal variations in seismic-noise source distribution by means of temporal variations in the correlation functions. Finally, we (a) provide a simple but accurate model for the seismic velocity variations observed at St. Eustatius, (b) investigate the relation between coseismic velocity drops observed at Saba with PGV, and (c) provide a simple model to (partly) remove the coseismic velocity drops at Saba from the observations.

## DATA COLLECTION

All seismic stations in the NA network (SABA, SABQ, and SABW on Saba, and SEUG, SEUS, and SEUT on St. Eustatius; Fig. 2) are equipped with a Streckeisen sensor of type STS-2 or STS-2.5, and a Quanterra datalogger of type Q330 or Q330S+ (de Zeeuw-van Dalfsen and Sleeman, 2018) to continuously record ground velocity at different sample rates. Throughout this article, we use the 40 samples per second data streams from vertical (BHZ) and horizontal components (BHN and BHE). All seismic stations except SEUG are located on the ground floor of concrete buildings without cellars or foundation cavities (e.g., cisterns) underneath. SEUG is deployed in a small, concrete vault of $1 \times 1$ m partly buried on a gently sloping hill.

The geology of Saba and St. Eustatius is very different: Saba is marked by Pelean andesite domes and lithified block and ash flows forming an irregular and very steep topography, whereas St. Eustatius is dominated by the symmetrical cone of The Quill, which deposited thick packages of loosely consolidated to unconsolidated material, especially in the flat-lying central part of the island (Roobol and Smith, 2004). Furthermore, the top of Mt. Scenery reaches 887 m whereas The Quill rises to "only" 600 m above sea level. At St. Eustatius, the groundwater table is located at about 55 m depth (see Data and Resources) below the upper geological strata. To our knowledge, no information on the groundwater depth at Saba is available.

On St. Eustatius, the seismometers are located on the lower slopes of The Quill (SEUG at 145 m and SEUT at 70 m) and on

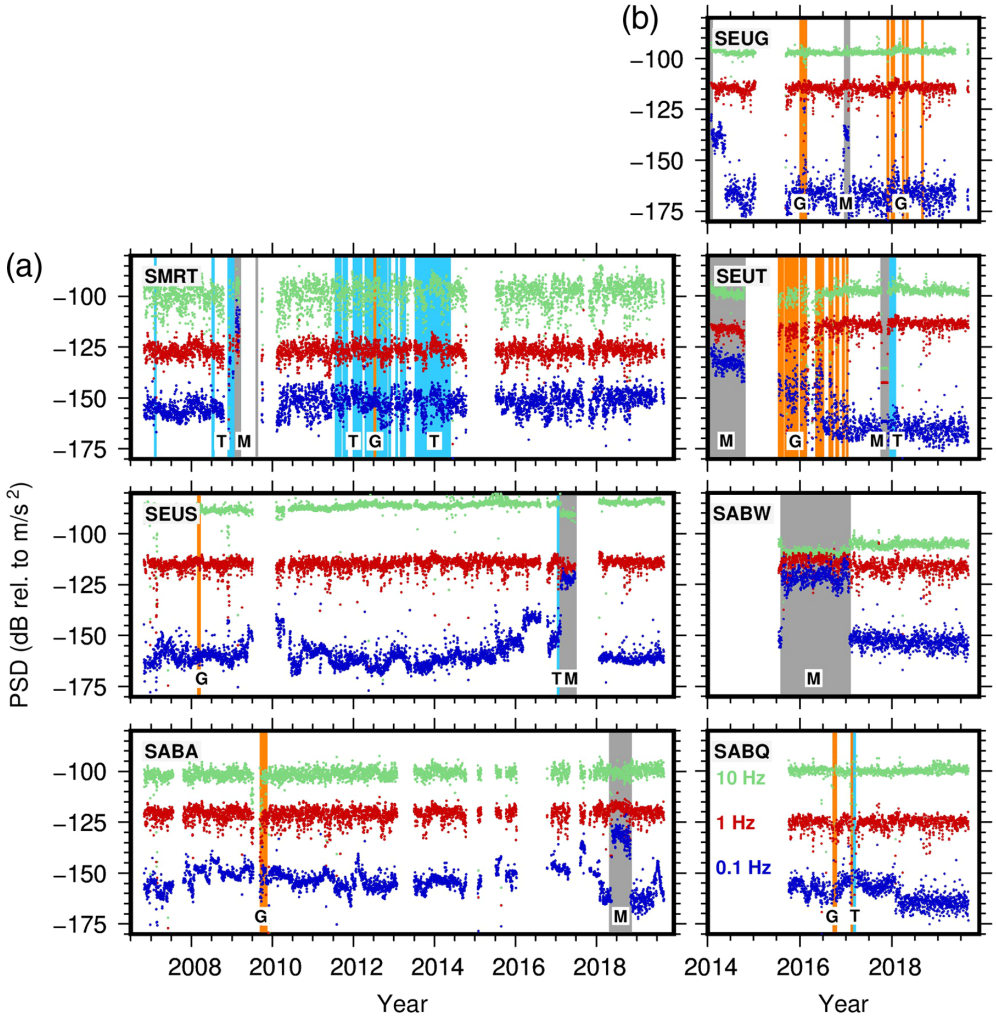


**Figure 3.** Temporal variations of the power spectral density (PSD) of the vertical ground acceleration recorded by (a) stations SMRT, SEUS, and SABA and (b) stations SEUG, SEUT, SABW, and SABQ, at 0.1, 1, and 10 Hz. The vertical bands indicate time windows with poor timing quality (indicated by T), a large number of data gaps (indicated by G), or with a tilted sensor (indicated by M, referring to the out-of-range mass position of the sensor). White bars indicate no data are available. The color version of this figure is available only in the electronic edition.

the flat-lying central part north of The Quill (SEUS at 40 m). On Saba, the instruments are located halfway between sea level and the top of Mt. Scenery scattered between the various domes (SABA at 320 m, SABQ at 235 m, and SABW at 400 m). The traverses between any two stations on Saba are characterized by irregular topography, whereas on St. Eustatius they are relatively smooth with less altitude variations. On St. Maarten, the seismometer is located on the ground floor of a concrete building constructed on a solid volcanic tuff outcrop at the top of St. Peter's hill (270 m), which is part of a larger mountain ridge.

Data quality is influenced, among others, by timing quality (phase differences), communication failure (data gaps), installation and site characteristics, and sensor tilting (waveform distortion). Figure 3 displays the data quality of the stations used in this article, from the initial deployment of each seismometer up to 1 September 2019, represented by the power spectral density of the vertical ground acceleration at 0.1, 1, and 10 Hz as a function of time (de Zeeuw-van Dalfsen and Sleeman, 2018). All time windows are shown, including data gaps, poor timing quality, and sensor tilting. Data from SEUS show a sudden and permanent increase in energy at around 1.19 and 1.24 Hz (Fig. 4) starting on 8 March 2013, most likely related to a mechanical source (e.g., air-conditioning) at the site. For this reason, data from stations SEUS, SEUG, and SEUT are discarded between 1.0 and 1.3 Hz.

## DATA PROCESSING

Our preprocessing discarded daily datafiles with (a) a significant (>40) number of gaps (one or more consecutive samples missing) and (b) data distortion by tilting of the sensor. We identified tilt by flagging data for which the daily mean of the raw data in counts exceeds 50% of the maximum output range of the datalogger. Data files for which the timing quality (provided by the datalogger through Global Positioning System signal reception) is below 50% are identified but used.

CCFs are calculated from daily data files following the workflow by Lecocq *et al.* (2014) in which (a) the time series are checked for timing issues to ensure sample alignment, (b) remaining data gaps up to 10 consecutive samples are filled by interpolation, (c) data are band-pass filtered between 0.05 and 14 Hz, and (d) amplitude spectra are prewhitened to increase the peakedness of the time series without affecting the phase. We computed CCFs per day for all station–component pairs in different frequency bands (0.4–1, 1.3–2.1, and 2–5 Hz) and averaged these by linear stacking over 10 days. A RefCC is calculated for each station–component pair by stacking CCFs over a year. Daily seismic velocity variations are then calculated using the moving-window cross spectrum (MWCS)

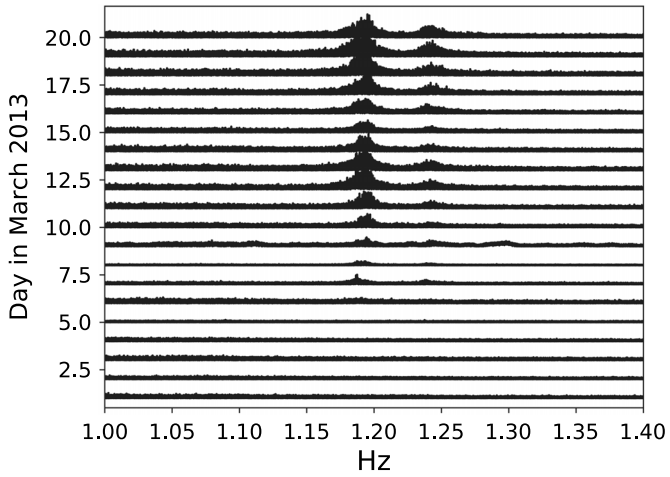


**Figure 4.** Spectral amplitudes (in counts) of vertical-component raw data from SEUS, recorded between 1 and 17 March 2013. The increase of energy at around 1.19 and 1.24 Hz started on 8 March 2013 and remained permanent over time since. Amplitudes are normalized with respect to the top trace.

technique (Poupinet *et al.*, 1984; Clarke *et al.*, 2011). MWCS measures the phase difference between a daily CCF and the RefCC as a function of lag time, and the slope of these pairs is the change dt in the travel time $t$. When assuming a homogeneous change in the medium, a change d$t$ in travel time $t$ relates directly to a change $dv$ in velocity $v$: $dv/v \approx -dt/t$.

Different frequency bands are used in various applications using ambient-noise cross-correlations depending on the interstation distances, the coherency of phases across the seismic network, and the subsurface depth that is being studied. De Siena *et al.* (2018) use a frequency band between 0.4 and 1.3 Hz to reconstruct period-dependent Rayleigh-wave group velocity maps for the Campi Flegrei caldera, and De Plaen *et al.* (2019) investigated the frequency band between 1 and 2 Hz to explore an improved ambient-noise monitoring strategy for Mt. Etna. A wider band, between 0.125 and 2 Hz, is used by Budi-Santoso and Lesage (2016) to investigate seismic velocity variations that occurred before the large eruption of Merapi Volcano in 2010, whereas Mordret *et al.* (2010) analyze data recorded at Mt. Ruapehu during eruptions in 2006 and 2007 between 0.2 and 0.7 Hz around the second microseism peak. There exists a pay off between using low- and high-frequency waves. Low-frequency waves penetrate deeper into the subsurface and thus will carry information from larger depths than high-frequency waves. On the other hand, the spatial resolution of low-frequency waves is less compared with higher frequency waves, which may prevent the detection of localized, temporal variations of subsurface seismic properties.

As no prior seismic velocity information about the subsurface is known at both Saba and St. Eustatius, we first investigate the characteristics of the CCFs as a function of frequency. Each daily CCF is correlated with a corresponding RefCC in a sliding window of length 12.5 s, starting at −86.25 s and running until 86.25 s. For each sliding window, we calculated the average and standard deviation of the correlation values between the daily CCFs and the RefCC. Figure 5 shows an example of the RefCC and the mean correlation between the daily CCFs and the RefCC, as well as the standard deviation, as a function of time of the sliding window. The example is for vertical-component data from SABA and SABW in three frequency bands (0.4–1, 1.3–2.1, and 2–5 Hz). In the high-frequency band, the daily CCFs and the RefCC are much less correlated (correlation 0.7 at $t = 0$) compared with the middle- and low-frequency bands (correlations 0.9 and 0.96, respectively). Other station–channel combinations show similar decorrelation in the high-frequency band. We assume the decorrelation is caused by the relatively large interstation distance (~2 km) compared to the wavelengths in this frequency band. The high-frequency noise waves most likely are of anthropogenic origin and decay rapidly within the interstation distance. We therefore decide not to use the high-frequency band during further analysis. In the low- and middle-frequency bands, we

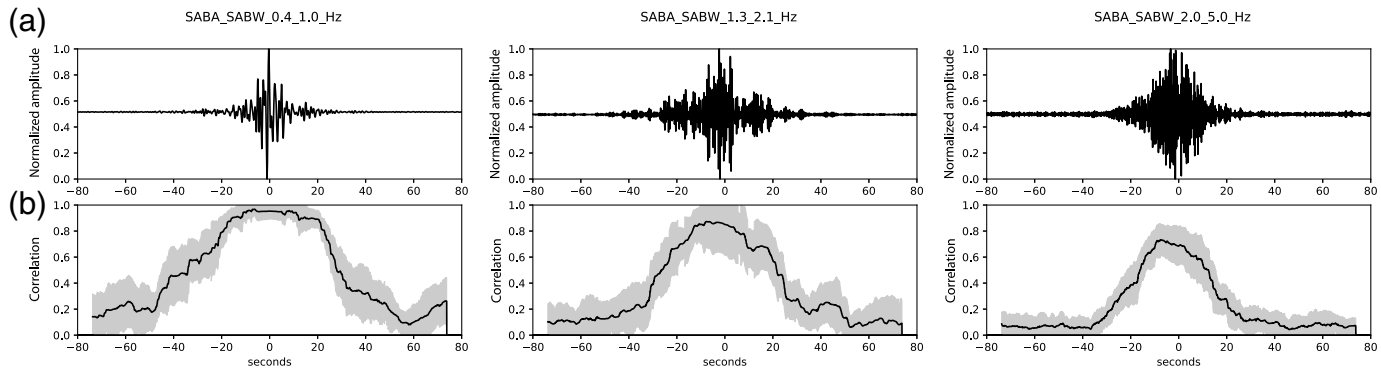


**Figure 5.** (a) Reference cross-correlation (RefCC) and (b) correlations between daily cross-correlation functions and RefCC from vertical-component recordings from SABA and SABW, with mean in black and standard deviation in gray, from 1 January 2017 to 31 August 2019 in frequency bands 0.4–1 Hz (left), 1.3–2.1 Hz (middle), and 2–5 Hz (right). RefCC is composed of data between 20 August 2017 and 5 May 2018.

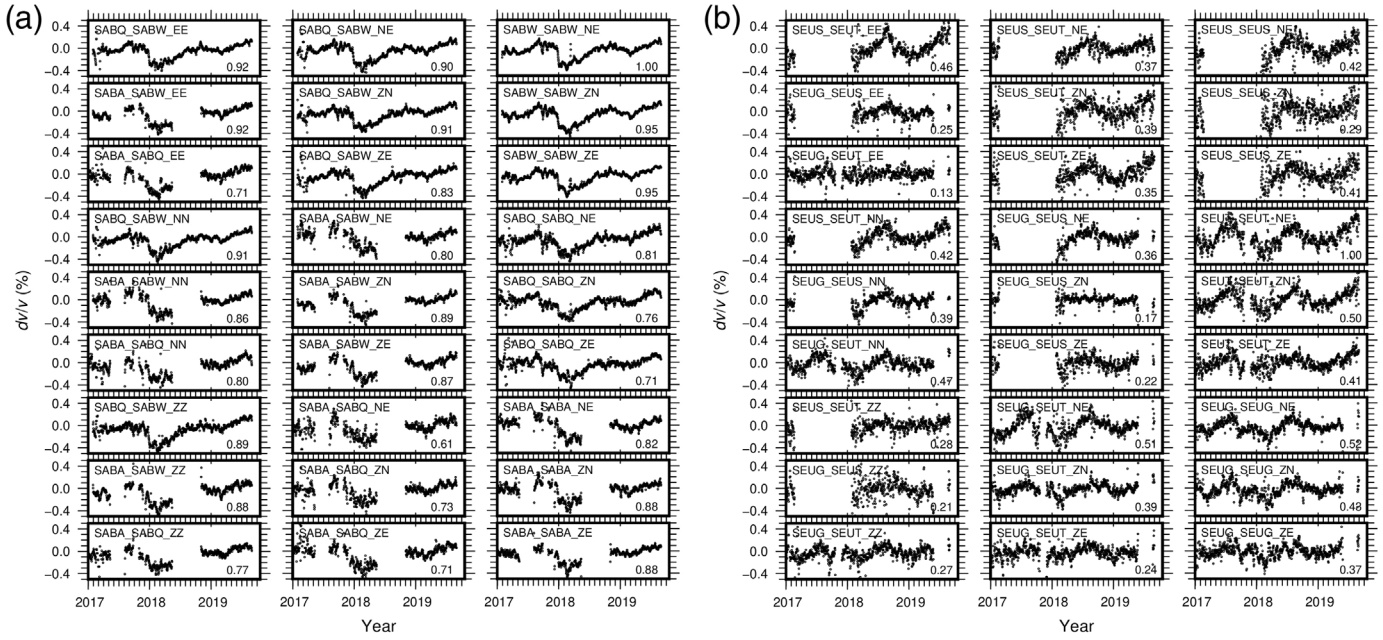


**Figure 6.** Velocity variations $dv/v$ derived from cross-correlations of the three-component ground-motion recordings from stations (a) SABA, SABQ, and SABW and (b) SEUG, SEUS, and SEUT, between 30 January 2017 and 1 September 2019, filtered between 1.3 and 2.1 Hz, and stacked over 10 days. RefCC is calculated from 1 August 2018 until 1 August 2019. Curves in the left columns are from cross-station similar-component correlations, in the middle columns from cross-station cross-component pairs, and in right columns for single-station cross-component combinations. The number in the lower right corner of each frame is the correlation coefficient with SABW_SABW_NE (for a) and SEUT_SEUT_NE (for b).

choose to only use the part of the CCFs for which the correlation with the RefCC is above 0.85, which roughly corresponds to a window length of about 25 s in both positive and negative lag directions. Rejection of data can also be controlled by the delay between the CCF and the RefCC in the MWCS processing. We did not put a priori strong restrictions here and allowed a delay of 0.4 s, which corresponds with a change in $dv/v$ of 1.6%.

## DATA ANALYSIS

For the low- and middle-frequency bands, we compare CCFs from SCs with CCFs from station pairs, hereafter called cross-station cross components (CCs). Within this study, we use half of the possible CC pairs (ZN, ZE, and NE) assuming the differences with the mirror components (NZ, EZ, and EN) in terms of $dv/v$ are negligible. Therefore, per three stations we have nine SCs (e.g., SABQ_BHE_SABQ_BHN) and 18 CCs. The 18 CCs hold nine CC pairs (e.g., SABA_BHN_SABQ_BHZ) and nine cross-station similar-component pairs (e.g., SEUG_BHZ_SEUT_BHZ).

From this analysis, we select the frequency band that optimizes similarities between the two types of correlation and justifies the use of SC as proxy for CC. Figure 6 displays the velocity variations $dv/v$ derived from these 27 correlations in the middle-frequency band (1.3–2.1 Hz), both for Saba and St. Eustatius, between 30 January 2017 and 1 September 2019.

The long-term velocity variations are remarkably similar to each other and show an annual cycle. The numbers in the lower right corners are the similarity (correlation coefficients) of the $dv/v$ with the velocity variation derived from an SC (in these examples, SABW_BHN_SABW_BHE and SEUT_BHN_SEUT_BHE). For the Saba stations, all 27 velocity variations are similar with correlation coefficients between 0.61 and 0.95 in this example, whereas for the stations on St. Eustatius this is between 0.13 and 0.52. The observed similarity between $dv/v$ from CC with $dv/v$ from SC supports the conclusion by De Plaen *et al.* (2016) that the noise cross-correlation technique may be successfully applied using one three-component seismometer only, for example, on volcanoes equipped with only one or a few instruments.

The histogram in Figure 7 shows the correlation coefficients between velocity variations, for both the low- and middle-frequency bands, derived from all possible station–channel pairs for the networks on Saba and St. Eustatius. The stacking over 10 days could potentially hide velocity changes on a shorter timescale. We tested different numbers of days for stacking (e.g., 1, 5, 10, and 30) and chose a length of 10 days to suppress small, daily variations of $dv/v$. It is reasonable to expect that significant changes at timescales less than 10 days still will be visible in the 10-day stack. At the same time, this choice will reveal more details in changes at longer timescales than stacking over 30 days or more. The time window for constructing the RefCCs is from 1 August 2018 to 1 August 2019, like in Figure 6. We selected this time window of 1 yr length based

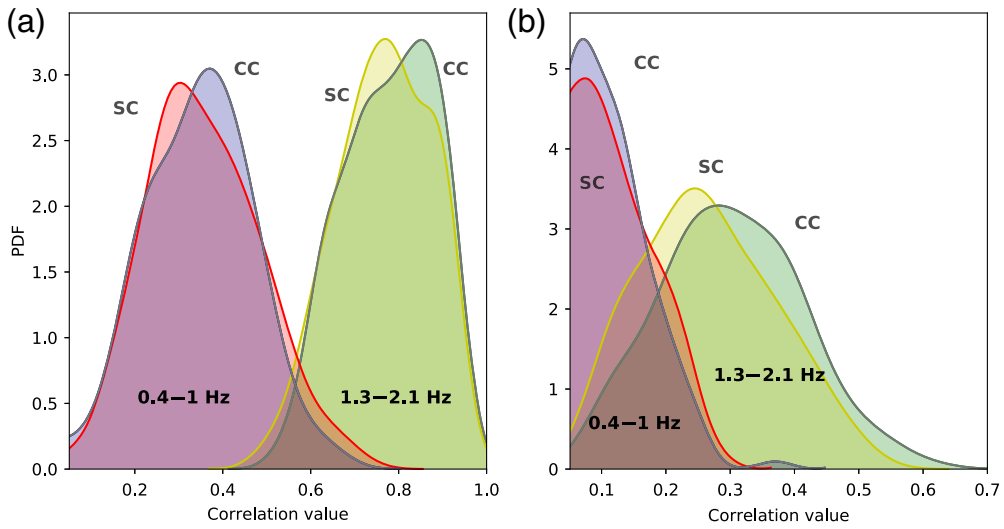


**Figure 7.** Distribution of the correlation coefficients between (1) cross station $dv/v$ with each other (CC), and (2) single station $dv/v$ and cross station $dv/v$ (SC), for (a) Saba and (b) St. Eustatius, in two frequency bands: 0.4–1 Hz and 1.3–2.1 Hz. The color version of this figure is available only in the electronic edition.

on the data quality assessment presented in Figure 3. In this time window, there are relatively stable levels of noise at 0.1, 1, and 10 Hz without long gaps, timing issues, or large tilts of any sensor. For Saba, the mean correlation is $0.82 \pm 0.09$ for the middle-frequency band and $0.36 \pm 0.16$ for the low-frequency band. For St. Eustatius, these values are $0.30 \pm 0.18$ and $0.13 \pm 0.18$, respectively. The histogram shows that for both Saba and St. Eustatius the SCs derived in the 1.3–2.1 Hz (middle) band will better represent the mean velocity variation measured by the network compared with the low-frequency band. Possibly at lower frequencies, the scattering is less effective, and therefore the estimate of the Green's function for collocated source and receiver becomes less reliable. Therefore, we will use the middle-frequency band to reliably estimate the velocity variations derived from a single station using data from 2006 to 2016.

Figure 8 presents $dv/v$ derived from the correlation of 13 yr of data. Before 2016, the velocity variations are derived from single stations (SCs from SABA, SEUS, and SMRT), whereas from 2016 onward the velocity variations are measured using all available cross-correlations (CCs and SCs) at Saba and St. Eustatius. The velocity variations derived from the SCs and CCs are plotted with the daily mean superimposed on top. The increased number of cross-correlations on Saba and St. Eustatius (3 per island before 2006 and 27 per island after 2016) reduces the variance in the mean. However, the results from the SCs (before 2016) can be used successfully to estimate the mean $dv/v$ derived from the CCs (after 2015) as was shown in Figure 7.

Data from SMRT do not show trends, annual variations, or rapid changes in $dv/v$ in the subsurface of St. Maarten, neither in the high- or low-frequency bands. This may be related to low data quality due to noise by wind. More likely is that the wind that hits the concrete building and the satellite dish on top is the dominant source of noise, which violates the condition in the cross-correlation technique to have distributed noise sources around the sensor(s). Also, the location of the sensor on top of a mountain ridge could lead to topographic effects such as (de) focussing of seismic waves or resonance of the whole ridge (Massa *et al.*, 2014). We observe that for SMRT the cross-component CCFs correlate with the RefCC above 0.85 only in a much narrower time window, of about 5 s, compared with those for stations at Saba and St. Eustatius, in other words, data seem to decorrelate rapidly here. This implies that only small lag time windows can be used to derive the velocity change, resulting in the introduction of larger errors. For the previous reasons, we do not further investigate data from SMRT in the rest of this article.

Based on visual inspection, the variations at SEUS show an annual velocity change that is positive during the summer, between April and September, and negative in the winter from October to March. The yearly trend in the $dv/v$ time series is $0.008 \pm 5 \times 10^{-4}$%. In contrast, data from SABA are characterized by "rapid" coseismic velocity drops, indicated by the vertical gray lines, superimposed on less distinct annual variations. The trend of the velocity variation at Saba is $0.023 \pm 5 \times 10^{-4}$% per year, which may be slightly overestimated due to the large $dv/v$ change in 2007.

## VELOCITY VARIATIONS AND OBSERVATIONS

### Meteorological parameters

The annual periodicity in our observations suggests sources with an annual variation such as temperature, pressure, or sources of ambient-noise (Gong *et al.*, 2015). In general, seasonal seismic velocity variations may reflect changes in subsurface material properties, or can be a result of changes in wavefield properties (e.g., source distribution and noise level). Driving forces of seasonal variations of material properties may include atmospheric temperature, barometric pressure, wind speed, precipitation, and groundwater level. Unfortunately, we have little information about groundwater variations but since 2016 KNMI started the continuous acquisition and

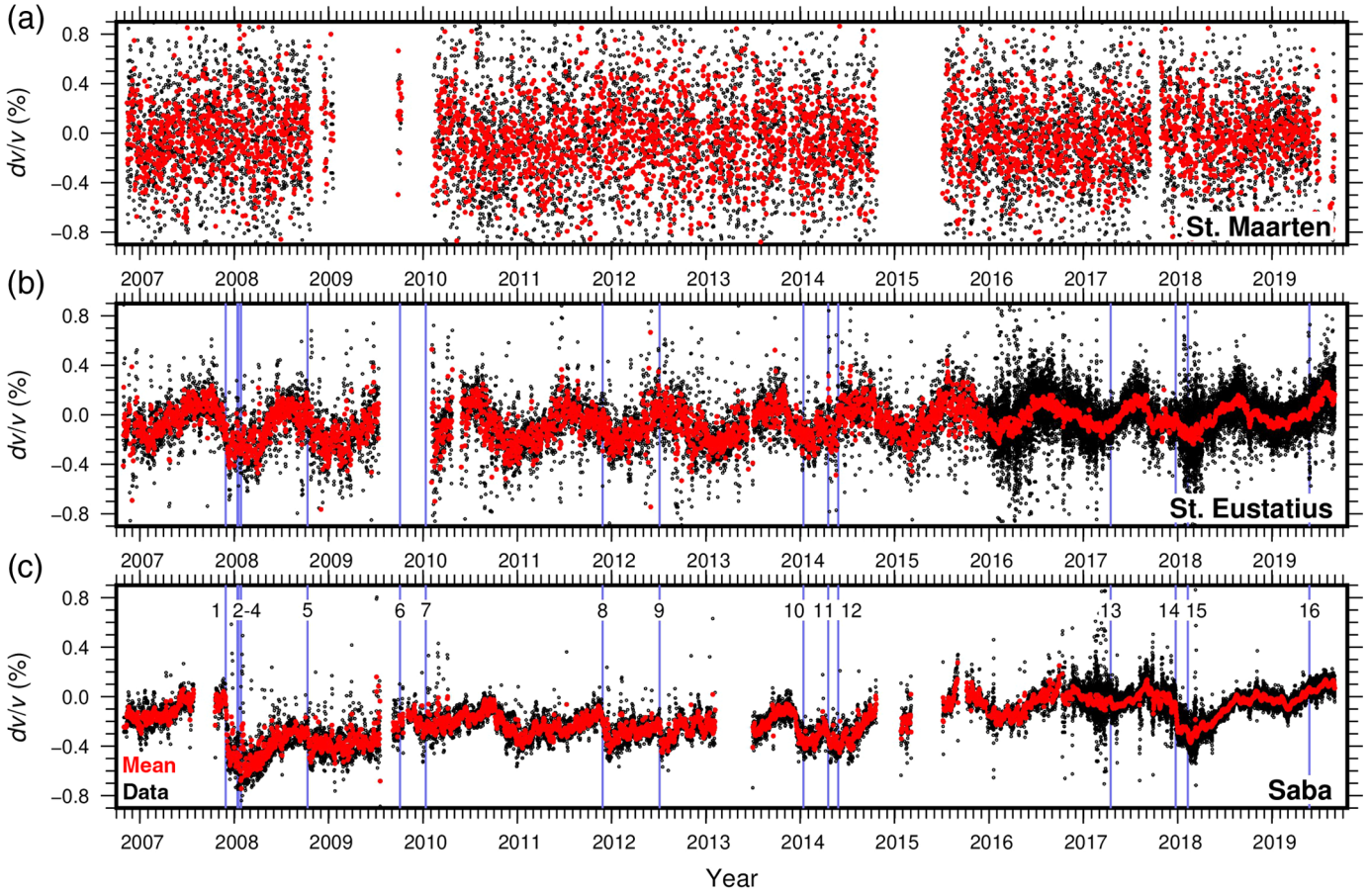


**Figure 8.** Velocity variations derived from all station–component cross-correlations at (a) St. Maarten, (b) St. Eustatius, and (c) Saba, in the frequency band 1.3–2.1 Hz and stacked over 10 days. All individual daily cross-component measurements are plotted (data), with the daily mean superimposed on top. Results for St. Maarten are based on SC correlations. Results for Saba and St. Eustatius are based on SC correlations until 2016, and based on all available SCs and CCs starting from 2016. Vertical lines with numbers indicate the occurrence of a significant earthquake in the region that was recorded by SABA with a peak ground velocity above 0.001 m/s in any component (Table 1). The color version of this figure is available only in the electronic edition.

collection of meteorological data (air temperature, atmospheric pressure, wind speed, wind direction, maximum wind speed, precipitation, and the number of sun hours), with a sample interval of 10 s, at the airports of Saba and St. Eustatius. These meteorological data are displayed in Figure 9.

Precipitation is very low and irregular (in location and time) on both islands throughout the years, and wind is relatively stable in both direction and speed. Clearly, the temperature fluctuations show the strongest annual variation, whereas the barometric pressure is rather stable with typically lower values during the hurricane season (August–November). Correlations between the velocity change and the meteorological data are shown in Figure 10 for lag times from −90 to 90 days, in which a negative lag time represents delay of the velocity change with respect to the meteorological parameter variation.

Seismic velocity variations correlate with air temperature for both Saba (0.53) and St. Eustatius (0.72). At these maximum values, the seismic velocity change at Saba is delayed with respect to air temperature for seven days, whereas at St. Eustatius this delay is four days.

The positive correlation between seismic velocity changes and temperature variations can be explained by thermally induced stress variations of the top layer (Richter *et al.*, 2014). With increasing air temperature, subsurface stress can be built up that can change the elastic properties such as the velocity of the upper-layer material. The high correlation value for St. Eustatius indicates that the seismic velocity changes due to thermal stress variations are much more pronounced there than for Saba. We suggest this variation is caused by the different geological characteristics of the islands.

## Illumination

To explore fluctuations in noise source distribution as a possible cause for the observed seasonal seismic velocity variations, we investigate the CCs and SCs for temporal variations in energy ratio between the causal and acausal part. When the noise sources are homogeneously distributed around

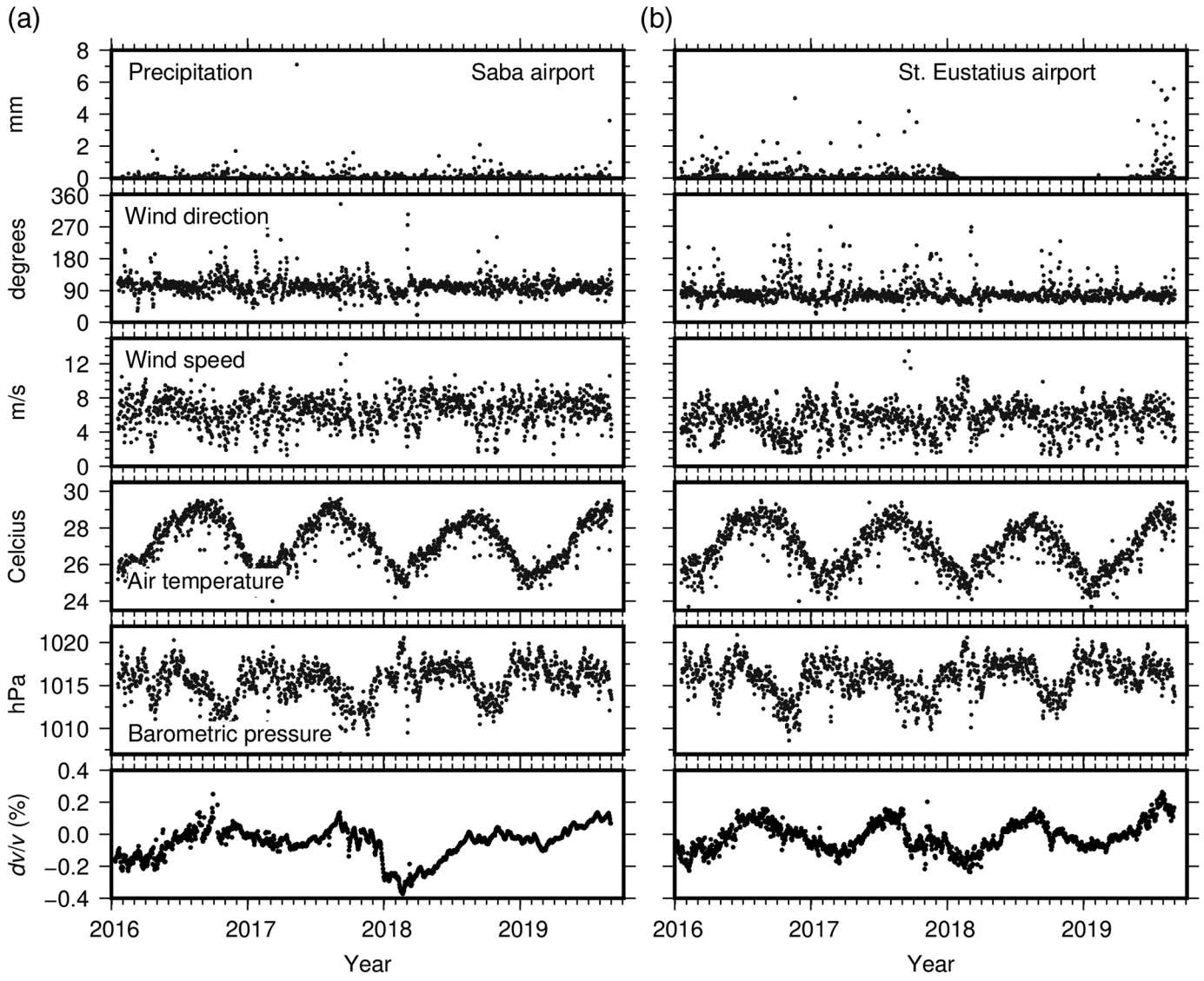


**Figure 9.** Velocity variations and meteorological measurements between 1 January 2016 and 1 September 2019 (a) for Saba and (b) for St. Eustatius. (From top to bottom) Precipitation, wind direction, wind speed, air temperature, atmospheric pressure, and the mean velocity variation (from Fig. 8).

two seismic stations, the energy flux between two stations is similar in both directions and the correlation function between the two stations is predominantly symmetrical in terms of energy (Stehly *et al.*, 2006). Energy flux asymmetry results from differences in the distribution of sources around the stations. As long as the distribution of sources remains stable in time, its pattern of energy ratio, which can be either asymmetrical or symmetrical, will not change. However, temporal fluctuations in the energy ratio may indicate temporal variations of noise source locations. We analyzed the temporal distribution of noise sources in relation to the annual seismic velocity variation by calculating the energy ratio of the causal and acausal part of the CCs as a function of time and then correlating the calculated energy ratio with the seismic velocity variation. Figure 11 shows the energy ratio at St. Eustatius calculated in two windows, a long window of 80 s duration starting from zero lag time, and one shorter window of 35 s length starting at 5 s lag time. The long window includes the direct waves, whereas the short window excludes the direct waves as well as late, multiple scattered waves. The energy ratios in both windows show some asymmetry (ratio $\neq 1$), which is rather stable over time. The correlation between the seismic velocity variations and the energy ratio between two stations (bottom panel) is small ($<0.2$) for both St. Eustatius and Saba, meaning that the observed annual seismic velocity variations cannot be explained by variations in noise source distribution.

The lack of distinct temporal variations in energy ratio implies stable distribution of noise sources around the seismic stations and/or homogeneous scattering properties of the shallow structure at the volcanoes that randomize the wavefield at 1.3–2.1 Hz. This suggests that the seismic velocity variations

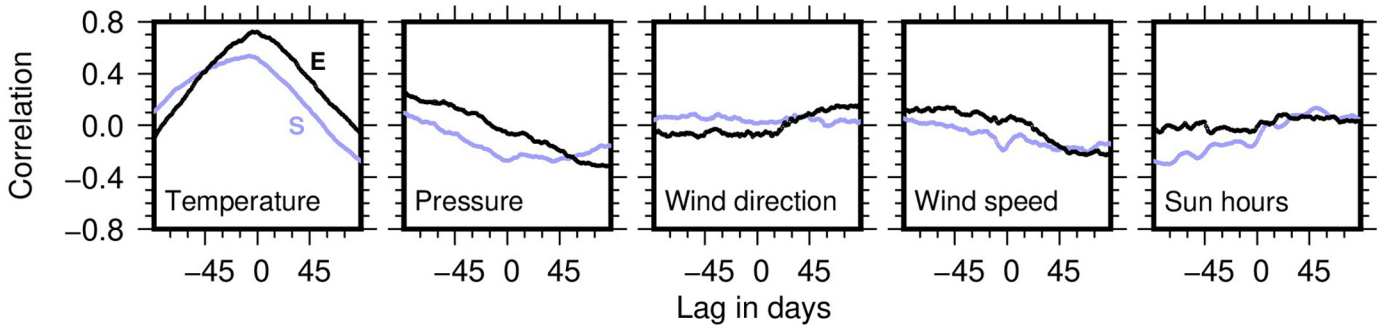


**Figure 10.** Correlation between the mean seismic velocity variations for Saba (S) and St. Eustatius (E) and the various meteorological parameters, using data from 2016 to 2019. Lag time represents time between the velocity variation and the meteorological data. The color version of this figure is available only in the electronic edition.

we observe are not related to annual variations in the noise sources but rather to genuine changes at shallow depth. Our data (Fig. 6) also show that the seismic velocity variations in time do not depend on the azimuth of station pairs on Saba. This supports the suggestion that the observed seismic velocity variations are not related to seasonal variations of the noise sources (Meier *et al.*, 2010) but to temperature-driven variations in the subsurface properties instead.

## Coseismic and cohurricane

We modeled the annual periodicity in the $dv/v$ observations for SEUS by a sine wave using SciPy (Virtanen *et al.*, 2020; see Data and Resources). The best fit was obtained with amplitude 0.1167%, angular frequency of $2\pi/365$ rad/day, phase offset of $-4\pi/3$ rad (relative to 1 January 2007) and $y$ offset of −0.051%:

$$dv/v_{\mathrm{mod}}(t) = -0.051 + 0.1167 \times \sin(2\pi/365 \times t - 4\pi/3), \quad (1)$$

in which $t$ is the day number since 1 January 2007. Figure 12 compares the model with the observations and shows the residuals in $dv/v$ after removal of the model values. The use of more seismic stations (cross-correlations), starting from 1 January 2016, decreases the residuals in $dv/v$ significantly (e.g., Hobiger *et al.*, 2012) with the standard deviation improving from 0.12% before 2016, to 0.05% after 2016. After removal of the annual variations a coseismic drop of about 0.19% is visible at the time of the largest earthquake (number 1 in Table 1), in 2007. No clear annual variation remains visible in the residuals.

Three temporary decreases in seismic velocity are visible (vertical bars marked by "H" in Fig. 12), one in each third quarter of 2016, 2017, and 2018. All are preceded by the passage of a category 4 or 5 hurricane (see Data and Resources): (1) Mathew of category 5 (28 September 2016–9 October 2016), (2) Irma of category 5 (30 August 2017–12 September 2017) followed by (3) Maria of category 5 (16–30 September 2017), and (4) Florence of category 4 (31 August 2018–17 September 2018) (Fig. 13). The $dv/v$ changes coinciding with Irma, Maria, and Florence are beyond two standard deviations from the mean (0.041%), whereas the change coinciding with Mathew is in the order of one standard deviation from the mean. This difference can be explained by the distance between each track path and St. Eustatius during the days of the highest intensity of the hurricane: Irma at 20 km, Maria at 140 km, Florence at 780 km, and Mathew at about 1500 km. Currently, the process behind the relation between the passage of a category 4–5 hurricane and the decrease in $dv/v$ is not well understood. No increase of precipitation is visible during the passage of the hurricanes

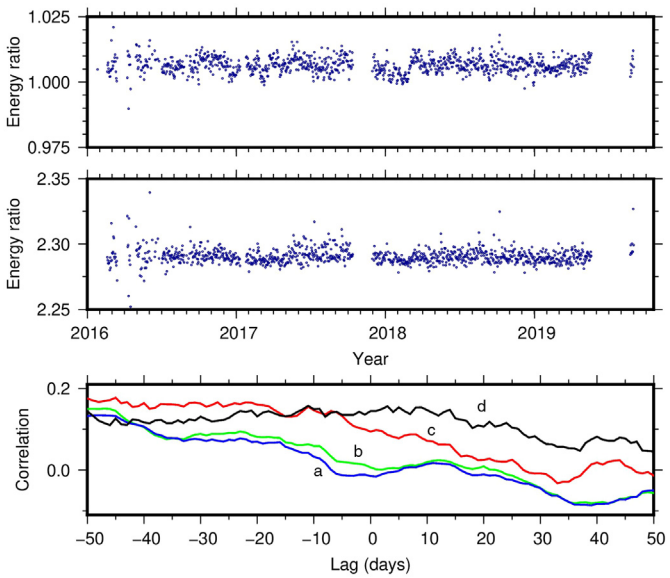


**Figure 11.** Energy ratio between the causal and acausal part of the CCs (SEUG_SEUT_ZZ) as a function of time in a long time window of 80 s length around zero lag (top panel), and in a short window of 35 s length starting at 5 s lag time (middle panel). The bottom panel shows the correlation between the energy ratio of the causal and acausal part of the CCs and the seismic velocity (2016–2019) measured between SABQ_SABW and SEUG_SEUT, ZZ components. (a): SABQ_SABW, 35 s; (b): SABQ_SABW, 80 s; (c): SEUG_SEUT, 80 s; and (d): SEUG_SEUT, 35 s. The color version of this figure is available only in the electronic edition.

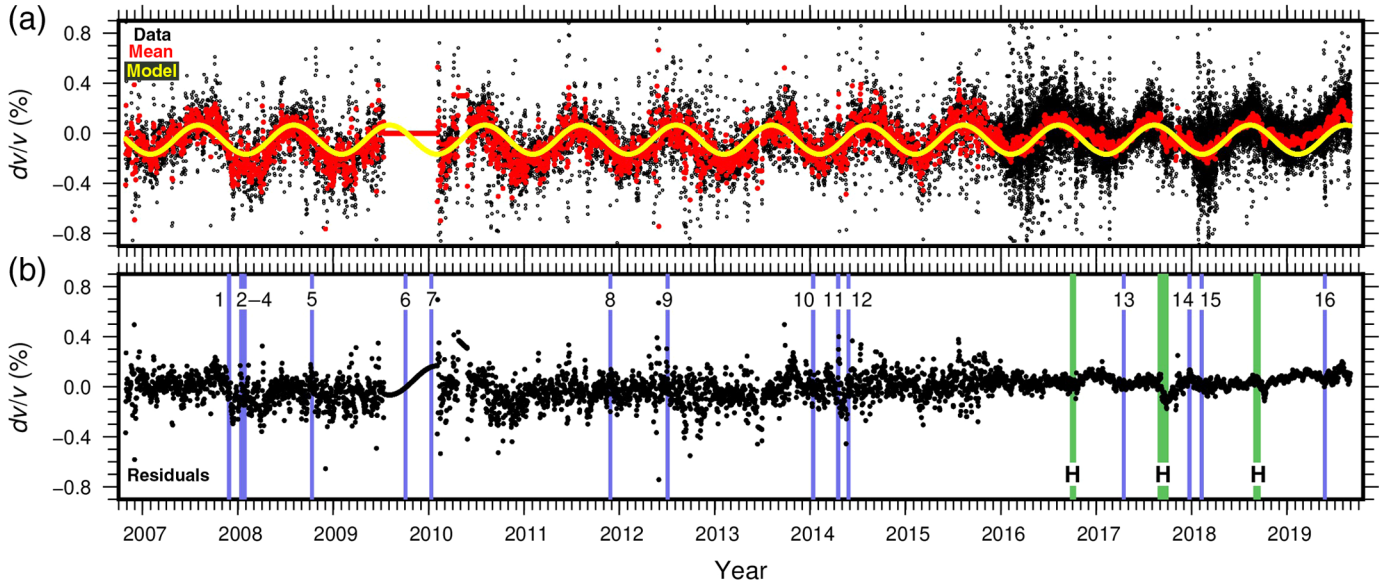


**Figure 12.** (a) Model of the velocity variations at St. Eustatius ("model") and the daily mean ("mean") of all $dv/v$ pairs ("data"). (b) The residuals between the daily mean $dv/v$ values and the model are shown. Numbered vertical lines indicate the earthquakes (Table 1); the vertical bars marked by "H" in 2016–2018 indicate the passage of hurricanes Mathew, Irma, Maria, and Florence. The color version of this figure is available only in the electronic edition.

(Fig. 13), but a correlation with barometric pressure seems plausible. However, the observation that this change in $dv/v$ is unrelated to volcanic activity is important for volcano monitoring. For the purpose of volcano monitoring, it is crucial to identify characteristics in the $dv/v$ base level that are not related to volcanic activity but may be related to external processes, such as the passage of a hurricane.

At station SABA, we observe clear coseismic velocity drops coinciding with the occurrence of regional earthquakes (Table 1), followed by postseismic recovery at different timescales. Elastic moduli (shear and bulk) of heterogeneous materials such as rocks and volcanic deposits are not constant in time (e.g., Sens-Schönfelder and Eulenfeld, 2019). The elastic nonlinearity of such heterogeneous materials causes the elastic moduli to change with the applied stress and pore pressure. Changes in these moduli will affect the seismic velocities as they depend on them. A variation in seismic velocity will thus reflect a change in subsurface stress or strain, which is

TABLE 1
**Earthquakes Recorded by SABA with Peak Ground Velocity (PGV) > 0.001 m/s**

| Number | Date/Time (yyyy/mm/dd hh:mm:ss) (UTC) | Latitude (°) | Longitude (°) | Depth (km) | $m_b$ | PGV (m/s) | $dv/v$ (%) |
|---|---|---|---|---|---|---|---|
| 1 | 2007/11/29 19:00:20 | 14.944 | −61.274 | 156 | 7.4 | $8.44 \times 10^{-3}$ | −0.49 |
| 2 | 2008/01/14 | — | | | | $3.16 \times 10^{-3}$ | −0.11 |
| 3 | 2008/01/17 | — | | | | $1.42 \times 10^{-3}$ | 0 |
| 4 | 2008/01/27 | — | | | | $1.86 \times 10^{-3}$ | 0 |
| 5 | 2008/10/11 10:40:14 | 19.194 | −64.826 | 26 | 5.9 | $4.44 \times 10^{-3}$ | −0.21 |
| 6 | 2009/10/05 16:28:10 | 18.021 | −62.853 | 42.9 | 4.7 | $1.61 \times 10^{-3}$ | 0 |
| 7 | 2010/01/12 21:53:10 | 18.382 | −72.588 | 15 | 6.6 | $2.30 \times 10^{-3}$ | 0 |
| 8 | 2011/11/28 10:35:57 | 19.098 | −66.747 | 15 | 5.1 | $1.62 \times 10^{-3}$ | −0.19 |
| 9 | 2012/07/04 21:29:26 | 18.120 | −62.983 | 94 | 5.0 | $6.24 \times 10^{-3}$ | −0.23 |
| 10 | 2014/01/13 04:01:03 | 19.043 | −66.810 | 20 | 6.4 | $1.04 \times 10^{-3}$ | 0 |
| 11 | 2014/04/19 19:31:35 | 17.997 | −62.544 | 59 | 5.1 | $4.91 \times 10^{-3}$ | 0 |
| 12 | 2014/05/28 21:15:06 | 18.045 | −68.351 | 90 | 5.8 | $1.66 \times 10^{-3}$ | 0 |
| 13 | 2017/04/17 05:23:15 | 17.500 | −61.142 | 16 | 5.6 | $1.76 \times 10^{-3}$ | −0.09 |
| 14 | 2017/12/24 15:12.53 | 18.107 | −62.804 | 73 | 4.8 | $3.11 \times 10^{-3}$ | −0.22 |
| 15 | 2018/02/09 17:43:37 | 18.632 | −61.977 | 43 | 5.2 | $2.46 \times 10^{-3}$ | −0.10 |
| 16 | 2019/05/26 08:31:13 | 19.170 | −64.640 | 52 | 3.0 | $2.29 \times 10^{-3}$ | −0.03 |

From these 16 earthquakes, 13 were reported by the U.S. Geological Survey and/or European-Mediterranean Seismological Centre between 1 January 2016 and 1 August 2019 in the region between 49°–83° W and 9°–27° N. In cases in which $dv/v = 0$, we could not clearly identify a significant seismic velocity change.

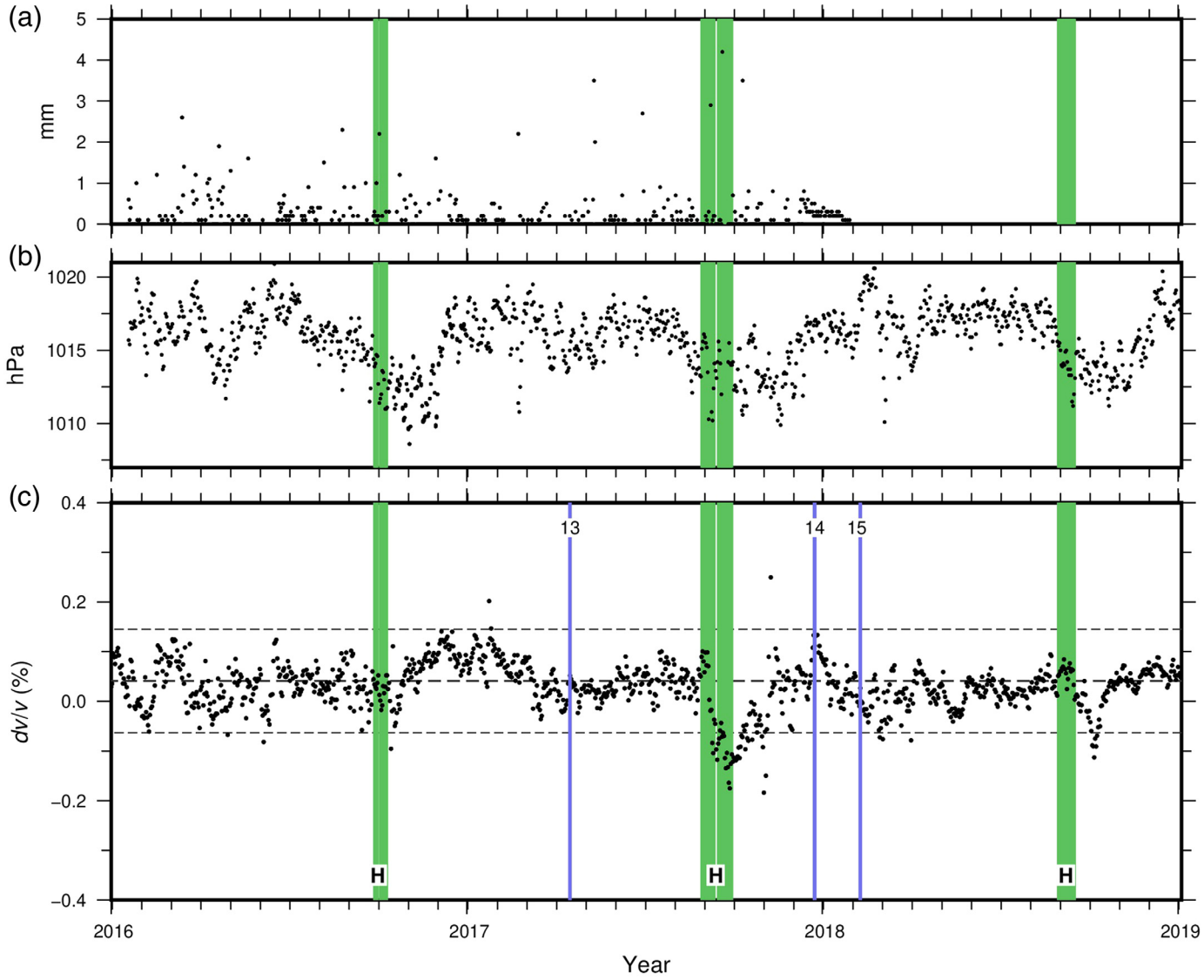


**Figure 13.** Detail of (a) the precipitation, (b) barometric pressure, and (c) the $dv/v$ at St. Eustatius after the passage (vertical bars indicated by "H") of hurricanes Mathew in 2016, Irma and Maria in 2017, and Florence in 2018. The horizontal, dashed lines represent the mean $dv/v$ and the levels of two standard deviations from the mean. The numbered vertical lines in (c) represent the occurrence of earthquakes (Table 1). The color version of this figure is available only in the electronic edition.

extremely important in volcano monitoring. The use of seismic velocity variations as proxy for subsurface stress or strain changes has been studied after earthquakes with coseismic velocity drops (e.g., Hobiger *et al.*, 2016; En-Jui *et al.*, 2019). The suggestion is that strong ground shaking after an earthquake causes the opening, growth, and closing of cracks in the medium, and also affects fluid level fluctuations in pores and cracks. This implies a relation between the observed coseismic velocity change and the ground acceleration that forces the change in the medium. To corroborate this, we used $\mathrm{PGV} \times 2\pi \times f_0$ as proxy for the ground acceleration, with $f_0$ the center frequency of the frequency band in which we calculate PGV. We investigated 10 frequency bands, each with a width of one-fifth of a decade, between 0.1 and 10 Hz.

We extracted PGV values from the SABA recordings for each day on which an earthquake with $\mathbf{M} > 4.5$ was reported by the U.S. Geological Survey (USGS) between 1 January 2016 and 1 August 2019 in the region between 49°–83° W and 9°–27° N. In total, 12 events were recorded by SABA, all with a peak velocity above 0.001 m/s in any component (Table 1). Also, we parsed our waveforms on PGV > 0.001 m/s and found one additional earthquake (14) that was reported by the European-Mediterranean Seismological Centre, and three earthquakes (2, 3, 4) that were not reported by USGS or International Seismological Centre. For all events, we calculated the PGV from the three components: $\mathrm{PGV} = \sqrt{\mathrm{PGV}_\mathrm{N}^2 + \mathrm{PGV}_\mathrm{E}^2 + \mathrm{PGV}_\mathrm{Z}^2}$ in the 10 frequency bands.

We manually measured the velocity drop from the $dv/v$ time series from SABA after the occurrence of each earthquake.

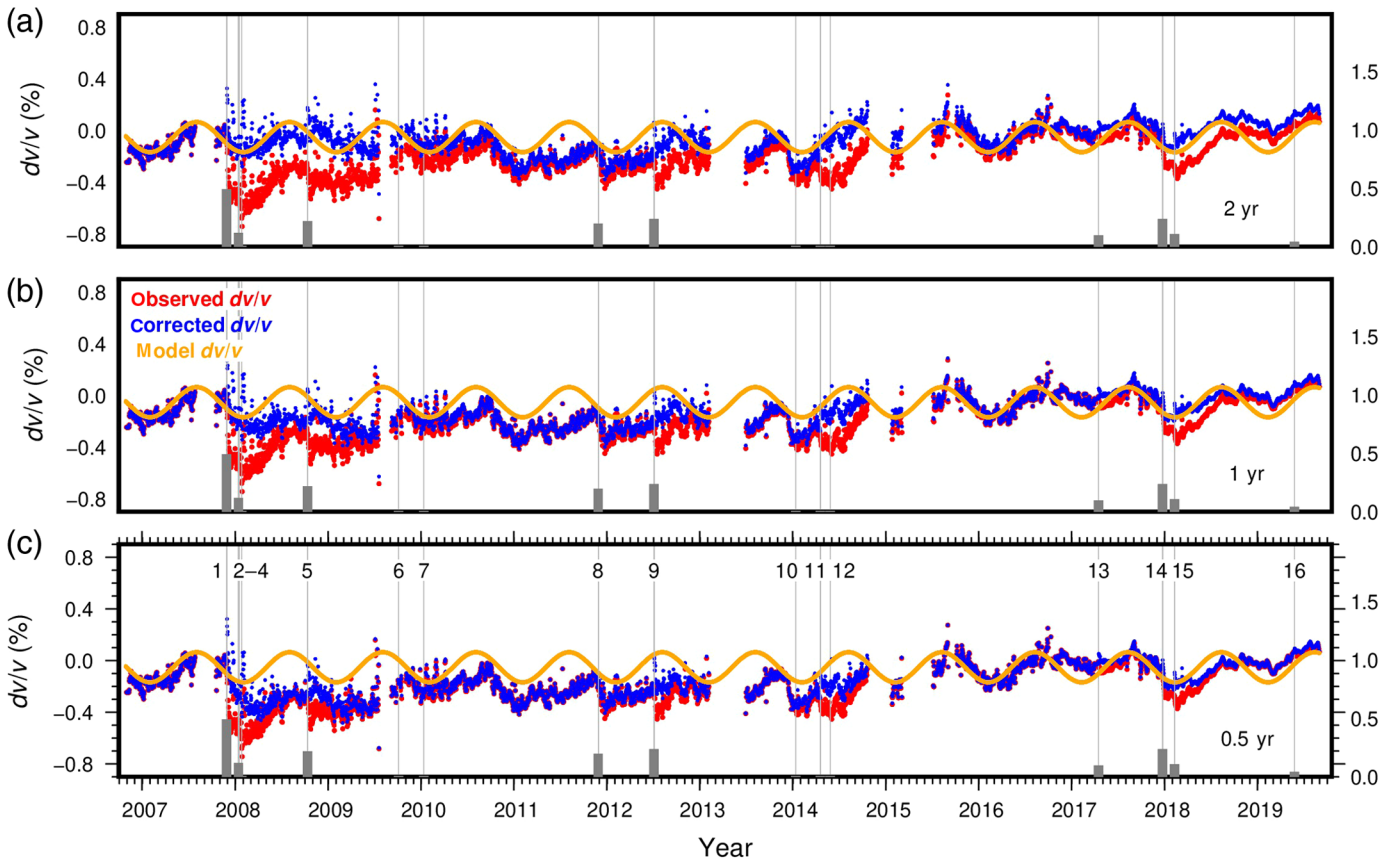


**Figure 14.** Velocity variations at SABA before ("observed") and after ("corrected") applying the correction for the coseismic velocity drop (equation 2). The sine curve ("model") is the velocity model for St. Eustatius (from Fig. 12). Decay times are (a) 2 yr, (b) 1 yr, and (c) six months. Bars on the bottom are the measured coseismic $dv/v$ values (right axes, in cm/s). The color version of this figure is available only in the electronic edition.

The first (and largest) event in 2007 shows a velocity drop of 0.49% (Fig. 8) that is about 2.5 times the observed velocity change of 0.19% at SEUS during the same event. This is in agreement with our observations that the subsurface velocity at Saba has a higher sensitivity to ground shaking than at St. Eustatius. Assuming that the factor 2.5 in sensitivity between Saba and St. Eustatius also holds during the other earthquakes, it explains why no other coseismic velocity drops are visible at St. Eustatius. Except for earthquake 14, for which the visible change in $dv/v$ (Fig. 13) remains questionable, all are below the standard deviation (of 0.12% before 2016 and of 0.05% after 2015).

We fitted $dv/v$ and PGV in each of the 10 frequency bands by linear regression. The slope, its error, and the correlation values are provided in Table 2. Our limited data set shows a good correlation of 0.78 between $dv/v$ and PGV around 1.29 Hz. At higher frequencies (>5 Hz), the correlation becomes poor (<0.4), whereas at lower frequencies the correlation remains moderate (around 0.6).

We used an exponential function (e.g., Hobiger *et al.*, 2016) to model the postseismic velocity recovery at SABA as a function of PGV at 1.29 Hz. The recovery time cannot be estimated easily due to the interference with other earthquakes; therefore, we tested three different decay times $T_d$ of 0.5, 1, and 2 yr, after which the $dv/v$ drop restored to within 10% of the initial value (which is in the order of the error in $dv/v$). By subtracting this

TABLE 2
**Slope and Its Error (in Percentage of Slope) of the Linear Regressions between $dv/v$ and Peak Ground Velocity (PGV) around the Center Frequency in Column 1 and the Correlation**

| PGV Center Frequency (Hz) | Slope *S* (%) | Std_err (%) | Correlation |
|---|---|---|---|
| 0.129 | −132.4 | 31.9 | 0.64 |
| 0.205 | −123.6 | 38.9 | 0.56 |
| 0.326 | −122.6 | 32.3 | 0.64 |
| 0.517 | −66.1 | 24.3 | 0.74 |
| 0.817 | −27.8 | 21.8 | 0.77 |
| 1.29 | −10.6 | 21.5 | 0.78 |
| 2.05 | −5.8 | 24.4 | 0.74 |
| 3.26 | −3.9 | 45.0 | 0.51 |
| 5.17 | −3.4 | 64.9 | 0.38 |
| 8.17 | −0.34 | 337.6 | 0.08 |

TABLE 3
**Correlations between the Sine Model (Equation 1) and $dv/v$ at St. Eustatius (Fig. 8), $dv/v$ at Saba (Fig. 8), and the Corrected $dv/v$ for Peak Ground Velocity (PGV) at 1.29 Hz with Recovery Times of 0.5, 1, and 2 yr at Saba (Fig. 14), in Three Different Time Periods, Respectively**

| $dv/v$ from | 2007–2010 | 2012–2015 | 2017–2019 |
|---|---|---|---|
| St. Eustatius | 0.65 | 0.57 | 0.81 |
| Saba | 0.32 | 0.42 | 0.55 |
| PGV 0.5 yr | 0.33 | 0.52 | 0.58 |
| PGV 1 yr | 0.36 | 0.57 | 0.68 |
| PGV 2 yr | 0.47 | 0.58 | 0.71 |

model from the observed $dv/v$, we get the corrected velocity variation $dv/v_{cor}$:

$$dv/v_{cor}(t) = dv/v(t) - 10.6 \times \mathrm{PGV}(t_i) \times H(t - t_i) \times \exp[(t - t_i) \times 365 \times k], \quad (2)$$

in which $t$ is time in days, $t_i$ is the day of earthquake $i$ and $H(t)$ is the Heaviside function with $H(t) = 0$ for $t < t_i$ and $H(t) = 1$ for $t \geq t_i$. Decay constant $k$ is defined by decay time $T_d : k = \ln(0.1)/T_d$. We compare in Figure 14 the $dv/v$ corrected for PGV with our $dv/v$ model for St. Eustatius (equation 1) and calculate the correlation between the corrected $dv/v$ and the sine model in three time windows (Table 3): (a) 2007–2010, based on SC, to analyze the effect of the largest earthquake (1); (b) 2012–2015, based on SC, to evaluate the decay time for smaller earthquakes (8–12), and (c) 2017–2019, based on CC.

A decay time of at least 2 yr is preferred in our model to recover the coseismic velocity drops in all time windows, as all correlations of $dv/v$ with the sine model increase with almost 0.2 compared with the correlation without the application of the seismic recovery (Table 3). The difference in the correlation in the three time windows, after correcting for the coseismic drops, suggests, however, that the recovery process may not be linearly related to $dv/v$, or PGV, and is more complex.

The corrected annual velocity changes for SABA (Fig. 14) also follow a sine although less pronounced than at St. Eustatius, as shown by the correlations in Table 3: 0.47 versus 0.65 between 2007 and 2010. From 2012 to 2015 and from 2017 to 2019, however, the sine model fits the corrected velocity changes at Saba much better, with correlations of 0.58 and 0.71, respectively. However, the correlation of the sine-wave model (equation 1) and the corrected $dv/v$ at Saba is lower than between the model and $dv/v$ at St. Eustatius. This difference is due to the higher sensitivity to earthquakes on Saba, as these earthquakes cause rapid drops in velocity followed by a recovery period that cannot be described uniformly. Furthermore, the distinctive geology of both islands may cause a different response to changes in meteorological conditions potentially resulting in different parameters for the best-fit sine wave.

## MONITORING

The use of the seismic-waveform cross-correlation technique is a valuable addition to existing volcano monitoring tools based on earthquake detection, ground deformation, and temperature measurements. At the same time, the implementation at volcano observatories as continuous monitoring tool is not widespread yet. L'Observatoire Volcanologique du Piton de La Fournaise (OVPF) has implemented seismic-noise analysis in their 24/7 volcano monitoring, although it does not yet play a central role (OVPF, personal comm., 2019). Possibly the challenge remains to better understand the velocity variations in relation to the underlying processes, in particular those variations occurring in times without volcanic activity. It is, therefore, extremely important to measure $dv/v$ during quiet times and analyze the observed features with the goal to attribute them to nonvolcanic sources.

The technique is based on waveform data from existing seismometers and does not require deployment of new types or sensors. The availability of continuously recorded data, in which the omnipresent ambient-noise is the carrier of information, makes the implementation of the cross-correlation technique in an operational 24/7 monitoring system a useful tool to monitor changes in the subsurface with high resolution (<0.1%) with a relatively small time delay (e.g., one day). We have shown the importance to (a) monitor $dv/v$ at times without volcanic activity, (b) extract a $dv/v$ base level for each volcano, and (c) understand the signal characteristics. This approach will help identify and separate changes in volcanic processes from significant deviative variations caused by nonvolcanic mechanisms.

An implementation of the $dv/v$ monitoring could track the velocity variation in two to three frequency bands on a daily basis and compare the new values with the predicted values from the models. Knowledge about known, nonvolcanic features could be expanded and added to the predictions in the model to make the monitoring system more reliable and less sensitive to $dv/v$ variations due to external sources. For Mt. Scenery and The Quill, we are working on the implementation of the correlation technique in the daily monitoring, based on our findings.

## DISCUSSION

We compared the results of SC and CC analysis and selected the frequency band (1.3–2.1 Hz) for which the highest similarity between SC and CC was achieved. This allowed us to extract a reliable $dv/v$ time series based on 13 yr of data and make a base level model for both Mt. Scenery and The Quill. Our preferred frequency band (1.3–2.1 Hz) will mostly carry information of subsurface seismic properties at shallow depths

(1–2 km). Smaller, shallow hydrothermal systems often amplify small temperature changes that have their origin at larger depth due to their limited capacity to accommodate for these changes (R. Moretti, personal comm., 2019). In such cases, we postulate that the monitoring of shallow depth may provide stronger signals in $dv/v$ than when monitoring at larger depth using lower frequencies. The presence of hot springs at Saba means that the hydrothermal system of Mt. Scenery reaches the surface and likely has a shallow component. It is, therefore, plausible that at Saba seismic velocity changes due to subsurface temperature changes could be detected very well in the selected frequency band. For St. Eustatius, the use of lower frequencies may be important to sample the deeper subsurface, which can be done using the same seismic recordings. For our purpose of exploring 13 yr of data, however, we restricted the analysis to the middle-frequency band, which justified the use of the SC approach to complement the cross-station technique starting from 2016.

Velocity variations at both Saba and St. Eustatius are positively correlating with air temperature, which suggests a mechanism similar to that described by Richter *et al.* (2014). The loosely consolidated to unconsolidated upper layer of volcanic material at St. Eustatius could introduce thermal stress variations that are less evident at Saba due to the different geology there. As currently no detailed information is available on the subsurface structures of both islands, it remains uncertain what exactly causes the difference in both amplitude as well as delay time of the correlations of velocity change and temperature. More work needs to be done to investigate the effect of variations of the sea surface temperature, which is delayed in time compared with the variations in atmospheric temperature, and the thermal coupling with the islands. At the same time, the difference in the sensitivity of the seismic velocity changes to PGV or PGA at both islands supports the assumption that different subsurface conditions such as geological features and effective pressure conditions (Ikeda and Tsuji, 2018) play an important role.

We modeled the main characteristic of $dv/v$ at St. Eustatius by a simple sine-wave model; however, the modeling for Saba remains more difficult due to the stronger sensitivity to ground shaking. The modeling of the coseismic velocity drops and the subsequent recovery through a simple linear relation between $dv/v$ and PGA with an exponential decay can only partly explain the observations, suggesting that a more complex, nonlinear model is required to describe the relation (e.g., Hobiger *et al.*, 2012). In contrast, at St. Eustatius the upper layer seems not to respond with significant permanent deformation after an earthquake likely due to the presence of unconsolidated material. More work is required to better understand the effect of strong amplitude events on the $dv/v$ with other approaches such as using phase cross-correlation (Schimmel, 1999; D'Hour *et al.*, 2016).

The current NA network provides good quality data that enable the noise correlation technique as a useful tool to monitor the subsurface at both volcanoes. Sampling the deeper interior of Mt. Scenery and The Quill could be done using lower frequencies; however, the correlation between all station–component pairs decreases significantly in the lower frequency band (Fig. 7), thus increasing the errors in the $dv/v$ estimates. An increase in the number of stations in the monitoring network would compensate for this, as has been shown in the high-frequency band for which the $dv/v$ standard deviation at Saba was reduced from 0.12% to 0.05%. The underlying assumption here is that different station-channel combinations measure the same medium change, which is not necessarily the case. Although data availability progressively improved over the years, the environmental conditions at both tropical islands affect the quality of continuous data significantly (Fig. 3). For the same reason, it is essential to extend the seismic network, so a minimum of three stations providing data at the same time is assured. Furthermore, the current network configuration is not optimally designed to encompass the volcanoes yet. We plan a first extension to this regard on Saba in early 2020, with an additional seismometer at the airport, and at St. Eustatius, at the end of 2020, an additional seismometer is planned on the southeast side of The Quill.

## CONCLUSIONS

We successfully applied the waveform cross-correlation technique to retrieve seismic velocity variations in the subsurface of volcanoes Mt. Scenery and The Quill after careful data selection. SC correlations have shown to be a proxy for cross-station correlations (CC) within the frequency band 1.3–2.1 Hz and provided a tool to establish a base level for the velocity variations in the (shallow) subsurface of both volcanoes, however, with larger errors than using CC with a small number of seismometers.

The velocity variations on St. Eustatius have a pronounced annual variation that highly correlates (0.72) with the atmospheric temperature and can be modeled by a simple sine function with amplitude 0.1167, angular frequency of $2\pi/365$ rad/day, and phase offset of $-4\pi/3$ rad. The subsurface velocity at St. Eustatius has a higher sensitivity to air temperature than at Saba. The correlation of the velocity variation with other meteorological parameters, ambient-noise variations, or seismic-noise distributions is negligible.

The observations on Saba are characterized by coseismic velocity drops (up to −0.49%) followed by recovery after earthquakes with local PGV $>$ 0.001 m/s. The subsurface velocity at Saba is more sensitive to ground shaking than at St. Eustatius. Our data set, although limited, suggests a linear relation between the coseismic velocity drop and PGV although more data are required to corroborate this. Recovery times could partly be modeled by a simple linear relation between the recovery process and PGV.

We believe seismic-noise cross-correlation monitoring could be a valuable addition to any volcano monitoring

network, providing a thorough analysis has been done (1) to establish a baseline of velocity changes and (2) to understand velocity changes unrelated to volcanic activity. In the case of Saba and St. Eustatius, our results are promising, although an expansion of the network would greatly improve the possibility to successfully identify velocity changes caused by future volcanic processes.

## DATA AND RESOURCES

All seismic data from network NA (doi: 10.21944/dffa7a3f-7e3a-3b33-a436-516a01b6af3f) used in this article are collected and owned by Royal Netherlands Meteorological Institute (KNMI; www.knmi.nl). Data are available through International Federation of Digital Seismograph Networks (FDSN) standardized webservices at KNMI: http://rdsa.knmi.nl/fdsnws/dataselect/1. Groundwater table information for St. Eustatius was retrieved from https://library.wur.nl/WebQuery/theses/directlink/2094045. Processing of data was done by MSNoise (Lecocq *et al.*, 2014; http://www.msnoise.org/), ObsPy (Beyreuther *et al.*, 2010), SciPy (Virtanen *et al.*, 2020), and Python (Python Software Foundation, https://www.python.org/). Fitting of data from SEUS was done by https://docs.scipy.org/doc/scipy/reference/generated/scipy.optimize.curve_fit.html. Information about the hurricanes was retrieved from https://www.nhc.noaa.gov/data/tcr/. The Generic Mapping Tools (GMT; Wessel *et al.*, 2013) and the Python data visualization library Seaborn (seaborn.pydata.org) were used for plotting of the figures. All websites were last accessed in May 2020.

## ACKNOWLEDGMENTS

The authors are grateful to Tim van Oosteren and his colleagues from Satel, and to Fernando Simmons from Eutel, for their continuous support in operating the seismic stations at Saba and St. Eustatius. The authors also thank George and Sally Works for their support to deploy seismic station SEUG. Operating the remote network NA would not have been possible without the continued support from the governments of Saba and St. Eustatius and the local support from Ellis Schmidt. In alphabetical order, the authors thank Hendrik-Jan Bosch, Leo Dogterom Verburg, Läslo Evers, Gert-Jan van den Hazel, Frits van de Peppel, Jan-Willem Schoonderwoerd, and Caron Vossen. Finally, the authors thank Bernard Dost, Elmer Ruigrok, and two anonymous reviewers for their valuable remarks to improve this article.

## REFERENCES

Allen, R. W., J. S. Collier, A. G. Stewart, T. Henstock, S. Goes, A. Rietbrock, and the VoiLA Team (2019). The role of arc migration in the development of the Lesser Antilles: A new tectonic model for the Cenozoic evolution of the eastern Caribbean, *Geology* **47,** no. 9, 891–895, doi: 10.1130/G46708.1.

Aoki, Y. (2015). Monitoring temporal changes of seismic properties, *Front. Earth Sci.* **3,** 42, doi: 10.3389/feart.2015.00042.

Ballmer, S., C. J. Wolfe, P. G. Okubo, M. M. Haney, and C. H. Thurber (2013). Ambient seismic noise interferometry in Hawai'i reveals long-range observability of volcanic tremor, *Geophys. J. Int.* **194,** no. 1, 512–523, doi: 10.1093/gji/ggt112.

Bennington, N., M. Haney, C. Thurber, and X. Zeng (2018). Inferring magma dynamics at Veniaminof Volcano via application of ambient noise, *Geophys. Res. Lett.* **45,** no. 21, 11,650–11,658, doi: 10.1029/2018GL079909.

Bensen, G. D., M. Ritzwoller, M. P. Barmin, A. Levshin, F. Lin, M. Moschetti, N. M. Shapiro, and Y. Yang (2007). Processing seismic ambient noise data to obtain reliable broad-band surface wave dispersion measurements, *Geophys. J. Int.* **169,** 1239–1260, doi: 10.1111/j.1365-246X.2007.03374.x.

Beyreuther, M., R. Barsch, L. Krischer, T. Megies, Y. Behr, and J. Wassermann (2010). ObsPy: A Python toolbox for seismology, *Seismol. Res. Lett.* **81,** 530–533, doi: 10.1785/gssrl.81.3.530.

Brenguier, F., D. Clarke, Y. Aoki, N. M. Shapiro, M. Campillo, and V. Ferrazzini (2011). Monitoring volcanoes using seismic noise correlations, *Compt. Rendus Geosci.* **343,** nos. 8/9, 633–638, doi: 10.1016/j.crte.2010.12.010.

Brenguier, F., N. M. Shapiro, M. Campillo, V. Ferrazzini, Z. Duputel, O. Coutant, and A. Nercessian (2008). Towards forecasting volcanic eruptions using seismic noise, *Nature Geosci.* **1,** no. 2, 126–130, doi: 10.1038/ngeo104.

Budi-Santoso, A., and P. Lesage (2016). Velocity variations associated with the large 2010 eruption of Merapi volcano, Java, retrieved from seismic multiplets and ambient noise cross-correlation, *Geophys. J. Int.* **206,** no. 1, 221–240, doi: 10.1093/gji/ggw145.

Caudron, C., T. Lecocq, D. K. Syahbana, W. McCausland, A. Watlet, T. Camelbeeck, and A. Bernard (2015). Stress and mass changes at a "wet" volcano: Example during the 2011-2012 volcanic unrest at Kawah Ijen volcano (Indonesia), *J. Geophys. Res.* **120,** 5117–5134, doi: 10.1002/2014JB011590.

Christman, A. R. (1953). Geology of St. Bartholomew, St. Martin, and Anguilla, Lesser Antilles, *Geol. Soc. Am. Bull.* **64,** 65–96, doi: 10.1130/0016-7606(1953)64[85:GOSBSM]2.0.CO;2.

Clarke, D., L. Zaccarelli, N. M. Shapiro, and F. Brenguier (2011). Assessment of resolution and accuracy of the moving window cross spectral technique for monitoring crustal temporal variations using ambient seismic noise, *Geophys. J. Int.* **186,** no. 2, 867–882, doi: 10.1111/j.1365-246X.2011.05074.x.

D'Hour, V., M. Schimmel, A. Do Nascimento, J. Ferreira, and H. L. Neto (2016). Detection of subtle hydromechanical medium changes caused by a small-magnitude earthquake swarm in NE Brazil, *Pure Appl. Geophys.* **173,** no. 4, 1097–1113, doi: 10.1007/s00024-015-1156-0.

De Plaen, R. S. M., A. Cannata, F. Cannavo, C. Caudron, T. Lecocq, and O. Francis (2019). Temporal changes of seismic velocity caused by volcanic activity at Mt. Etna revealed by the autocorrelation of ambient seismic noise, *Front. Earth Sci.* **6,** 251, doi: 10.3389/feart.2018.00251.

De Plaen, R. S. M., T. Lecocq, C. Caudron, V. Ferrazzini, and O. Francis (2016). Single-station monitoring of volcanoes using seismic ambient noise, *Geophys. Res. Lett.* **43,** 8511–8518, doi: 10.1002/2016GL070078.

De Siena, L., C. Sammarco, D. G. Cornwell, M. La Rocca, F. Bianco, L. Zaccarelli, and H. Nakahara (2018). Ambient seismic noise image of the structurally controlled heat and fluid feeder pathway at Campi Flegrei caldera, *Geophys. Res. Lett.* **45,** 6428–6436, doi: 10.1029/2018GL078817.

de Zeeuw-van Dalfsen, E., and R. Sleeman (2018). A permanent, real-time monitoring network for the volcanoes Mount Scenery and

The Quill in the Caribbean Netherlands, *Geosciences* **8,** no. 9, 320, doi: 10.3390/geosciences8090320.

Donaldson, C., C. Caudron, R. G. Green, W. A. Thelen, and R. S. White (2017). Relative seismic velocity variations correlate with deformation at Kīlauea volcano, *Sci. Adv.* **3,** no. 6, e1700219, doi: 10.1126/sciadv.1700219.

Draganov, D., K. Wapenaar, and J. Thorbecke (2006). Seismic interferometry: Reconstructing the earth's reflection response, *Geophysics* **71,** no. 4, SI61–SI70, doi: 10.1190/1.2209947.

Duputel, Z., V. Ferrazzini, F. Brenguier, N. Shapiro, C. M. A. Nercessian, M. Campillo, and A. Nercessian (2009). Real time monitoring of relative velocity changes using ambient seismic noise at the Piton de la Fournaise volcano (La Réunion) from January 2006 to June 2007, *J. Volcanol. Geoth. Res.* **184,** nos. 1/2, 164–173, doi: 10.1016/j.jvolgeores.2008.11.024.

En-Jui, L., P. Chen, D. Mu, R.-J. Rau, and C.-M. Lin (2019). Coseismic velocity variations associated with the 2018 $M_w$ 6.4 Hualien earthquake estimated using repeating earthquakes, *Seismol. Res. Lett.* **90,** no. 1, 118–130, doi: 10.1785/0220180230.

Fokker, E., and E. Ruigrok (2019). Quality parameters for passive image interferometry tested at the Groningen network, *Geophys. J. Int.* **218,** 1367–1378, doi: 10.1093/gji/ggz228.

Froment, B., M. Campillo, P. Roux, P. Gouedard, A. Verdel, and R. L. Weaver (2010). Estimation of the effect of nonisotropically distributed energy on the apparent arrival time in correlations, *Geophysics* **75,** no. 5, SA85–SA93, doi: 10.1190/1.3483102.

Garmon, W. T., C. D. Allen, and K. M. Groom (2017). Geologic and tectonic background of the Lesser Antilles, in *Landscapes and Landforms of the Lesser Antilles*, C. Allen (Editor), World Geomorphological Landscapes, Springer, Cham, Switzerland.

Gassenmeier, M., C. Sens-Schönfelder, M. Delatre, and M. Korn (2015). Monitoring of environmental influences on seismic velocity at the geological storage site for $CO_2$ in Ketzin (Germany) with ambient seismic noise, *Geophys. J. Int.* **200,** no. 1, 524–533.

Gong, M., Y. Shen, H. Li, X. Li, and J. Jia (2015). Effects of seasonal changes in ambient noise sources on monitoring temporal variations in crustal properties, *J. Seismol.* **19,** 781–790, doi: 10.1007/s10950-015-9494-z.

Groos, J. C., S. Bussat, and J. R. R. Ritte (2012). Performance of different processing schemes in seismic noise cross-correlations, *Geophys. J. Int.* **188,** no. 2, 498–512, doi: 10.1111/j.1365-246X.2011.05288.x.

Hable, S., K. Sigloch, G. Barruol, S. C. Stähler, and C. Hadziioannou (2018). Clock errors in land and ocean bottom seismograms: High-accuracy estimates from multiple-component noise cross-correlations, *Geophys. J. Int.* **214,** no. 3, 2014–2034, doi: 10.1093/gji/ggy236.

Hadziioannou, C., E. Larose, O. Coutant, P. Roux, and M. Campillo (2009). Stability of monitoring weak changes in multiply scattering media with ambient noise correlation: Laboratory experiments, *J. Acoust. Soc. Am.* **125,** no. 6, 3688–3695, doi: 10.1121/1.3125345.

Hanasoge, S. M. (2013). The influence of noise sources on cross-correlation amplitudes, *Geophys. J. Int.* **192,** no. 1, 295–309, doi: 10.1093/gji/ggs015.

Hillers, G., Y. Ben-Zion, M. Campillo, and D. Zigone (2015). Seasonal variations of seismic velocities in the San Jacinto fault area observed with ambient seismic noise, *Geophys. J. Int.* **202,** no. 2, 920–932, doi: 10.1093/gji/ggv151.

Hobiger, M., U. Wegler, K. Shiomi, and H. Nakahara (2012). Coseismic and postseismic elastic wave velocity variations caused by the 2008 Iwate-Miyagi Nairiku earthquake, Japan, *J. Geophys. Res.* **117,** no. B09313, doi: 10.1029/2012JB009402.

Hobiger, M., U. Wegler, K. Shiomi, and H. Nakahara (2016). Coseismic and post-seismic velocity changes detected by passive image interferometry: Comparison of one great and five strong earthquakes in Japan, *Geophys. J. Int.* **205,** no. 2, 1053–1073, doi: 10.1093/gji/ggw066.

Hong, T.-K., J. Lee, D. Chi, and S. Park (2017). Seismic velocity changes in the backarc continental crust after the 2011 $M_w$ 9.0 Tohoku-Oki megathrust earthquake, *Geophys. Res. Lett.* **44,** 10,997, doi: 10.1002/2017GL075447.

Hotovec-Ellis, A. J., J. S. Gomberg, J. E. Vidale, and K. C. Creager (2014). A continuous record of inter-eruption velocity change at Mount St. Helens from coda-wave interferometry, *J. Geophys. Res.* **119,** 2199–2214.

Ikeda, T., and T. Tsuji (2018). Temporal change in seismic velocity associated with an offshore $M_W$ 5.9 Off-Mie earthquake in the Nankai subduction zone from ambient noise cross-correlation, *Progr. Earth Planet. Sci.* **5,** 62, doi: 10.1186/s40645-018-0211-8.

Lecocq, T., C. Caudron, and F. Brenguier (2014). MSNoise, a python package for monitoring seismic velocity changes using ambient seismic noise, *Seismol. Res. Lett.* **85,** 715–726, doi: 10.1785/0220130073.

Machacca, R., P. Lesage, E. Larose, P. Lacroix, and R. Anccasi (2019). Detection of pre-eruptive seismic velocity variations at an andesitic volcano using ambient noise correlation on 3-component stations: Ubinas volcano, Peru, *J. Volcanol. Geoth. Res.* **381,** 83–100, doi: 10.1016/j.jvolgeores.2019.05.014.

Massa, M., S. Barani, and S. Lovati (2014). Overview of topographic effects based on experimental observations: Meaning, causes and possible interpretations, *Geophys. J. Int.* **197,** no. 3, 1537–1550, doi: 10.1093/gji/ggt341.

Maury, R. C., G. K. Westbrook, P. E. Baker, Ph. Bouysse, and D. Westercamp (1991). Geology of the Lesser Antilles, in *The Caribbean Region*, Vol. H, doi: 10.1130/DNAG-GNA-H.141.

Meier, U., F. Brenguier, and N. M. Shapiro (2010). Detecting seasonal variations in seismic velocities within Los Angeles basin from correlations of ambient seismic noise, *Geophys. J. Int.* **181,** no. 2, 985–996, doi: 10.1111/j.1365-246X.2010.04550.x.

Mordret, A., A. D. Jolly, Z. Duputel, and N. Fournier (2010). Monitoring of phreatic eruptions using interferometry on retrieved cross-correlation function from ambient seismic noise: Results from Mt. Ruapehu, New Zealand, *J. Volcanol. Geoth. Res.* **191,** nos. 1/2, 46–59, doi: 10.1016/j.jvolgeores.2010.01.010.

Nakata, N., and R. Snieder (2011). Near-surface weakening in Japan after the 2011 Tohoku-Oki earthquake, *Geophys. Res. Lett.* **38,** no. 17, doi: 10.1029/2011GL048800.

Olivier, G., F. Brenguier, R. Carey, P. Okubo, and C. Donaldson (2019). Decrease in seismic velocity observed prior to the 2018 eruption of Kīlauea volcano with ambient seismic noise interferometry, *Geophys. Res. Lett.* **46,** 3734–3744, doi: 10.1029/2018GL081609.

Poupinet, G., W. Ellsworth, and J. Frechet (1984). Monitoring velocity variations in the crust using earthquake doublets: An application to the Calaveras faults, California, *J. Geophys. Res.* **89,** 5719–5731.

Richter, T., C. Sens-Schönfelder, R. Kind, and G. Asch (2014). Comprehensive observation and modeling of earthquake and temperature related seismic velocity changes in northern Chile with passive image interferometry, *J. Geophys. Res.* **119,** 4747–4765, doi: 10.1002/2013JB010695.

Rivet, D., F. Brenguier, and F. Cappa (2015). Improved detection of preeruptive seismic velocity drops at the Piton de La Fournaise volcano, *Geophys. Res. Lett.* **42,** 6332–6339, doi: 10.1002/2015GL064835.

Roobol, M., and A. Smith (2004). *Volcanology of Saba and St. Eustatius, Northern Lesser Antilles*, Koninklijke Nederlandse Akademie van Wetenschappen, Amsterdam, The Netherlands.

Rubinstein, J. L., and G. C. Beroza (2005). Depth constraints on nonlinear strong ground motion from the 2004 Parkfield earthquake, *Geophys. Res. Lett.* **32,** no. 14, doi: 10.1029/2005GL023189.

Schimmel, M. (1999). Phase cross-correlations: Design, comparisons and applications, *Bull. Seismol. Soc. Am.* **89,** 1366–1378.

Sens-Schönfelder, C. (2008). Synchronizing seismic networks with ambient noise, *Geophys. J. Int.* **174,** no. 3, 966–970, doi: 10.1111/j.1365-246X.2008.03842.x.

Sens-Schönfelder, C., and T. Eulenfeld (2019). Probing the in situ elastic nonlinearity of rocks with earth tides and seismic noise, *Phys. Rev. Lett.* **122,** 138501, doi: 10.1103/PhysRevLett.122.138501.

Sens-Schönfelder, C., and U. Wegler (2006). Passive image interferometry and seasonal variations of seismic velocities at Merapi Volcano, Indonesia, *Geophys. Res. Lett.* **33,** L21302, doi: 10.1029/2006GL027797.

Shapiro, N. M., and M. Campillo (2004). Emergence of broadband Rayleigh waves from correlations of the ambient seismic noise, *Geophys. Res. Lett.* **31,** L07614, doi: 10.1029/2004GL019491.

Stehly, L., M. Campillo, and N. M. Shapiro (2006). A study of seismic noise from long-range correlation properties, *J. Geophys. Res.* **111,** doi: 10.1029/2005JB004237.

Stehly, L., M. Campillo, and N. M. Shapiro (2007). Traveltime measurements from noise correlation: Stability and detection of instrumental time-shifts, *Geophys. J. Int.* **171,** no. 1, 223–230, doi: 10.1111/j.1365-246X.2007.03492.x.

Virtanen, P., R. Gommers, T. E. Oliphant, M. Haberland, T. Reddy, D. Cournapeau, E. Burovski, P. Peterson, W. Weckesser, J. Bright, *et al.* (2020). SciPy 1.0: Fundamental algorithms for scientific computing in Python, *Nat. Methods* **17,** 261–272, doi: 10.1038/s41592-019-0686-2.

Wapenaar, K., and J. Fokkema (2006). Green's function representations for seismic interferometry, *Geophysics* **71,** no. 4, SI33–SI46, doi: 10.1190/1.2213955.

Wegler, U., H. Nakahara, C. Sens-Schönfelder, M. Korn, and K. Shiomi (2009). Sudden drop of seismic velocity after the 2004 Mw 6.6 mid-Niigata earthquake, Japan, observed with Passive Image Interferometry, *J. Geophys. Res.* **114,** no. B005869, doi: 10.1029/2008JB005869.

Wessel, P., W. H. F. Smith, R. Scharroo, J. Luis, and F. Wobbe (2013). Generic mapping tools: Improved version released, *EOS Trans. AGU* **94,** no. 45, 409–410, doi: 10.1002/2013EO450001.

Westerman, J., and H. Kiel (1961). *The Geology of Saba and St. Eustatius, with Notes on the Geology of St. Kitts, Nevis and Montserrat (Lesser Antilles)*, Natuurwetenschappelijke Studiekring voor Suriname en de Nederlandse Antillen, Utrecht, The Netherlands.

**Manuscript received 13 January 2020**
**Published online 16 June 2020**